Article

Influence of Synthesis Parameters on Structure and Characteristics of the Graphene Grown Using PECVD on Sapphire Substrate

Šarūnas Jankauskas [1] , **Šarūnas Meškinis** [1] , **Nerija Žurauskienė** [2] **and Asta Guobienė** [1,*]

1 Institute of Materials Science, Kaunas University of Technology, K. Baršausko St. 59, LT-51423 Kaunas, Lithuania; sarunas.jankauskas@ktu.lt (Š.J.); sarunas.meskinis@ktu.lt (Š.M.)
2 Department of Functional Materials and Electronics, Center for Physical Sciences and Technology, Saulėtekio av. 3, LT-10257 Vilnius, Lithuania; nerija.zurauskiene@ftmc.lt
* Correspondence: asta.guobiene@ktu.lt

Abstract: The high surface area and transfer-less growth of graphene on dielectric materials is still a challenge in the production of novel sensing devices. We demonstrate a novel approach to graphene synthesis on a C-plane sapphire substrate, involving the microwave plasma-enhanced chemical vapor deposition (MW-PECVD) technique. The decomposition of methane, which is used as a precursor gas, is achieved without the need for remote plasma. Raman spectroscopy, atomic force microscopy and resistance characteristic measurements were performed to investigate the potential of graphene for use in sensing applications. We show that the thickness and quality of graphene film greatly depend on the CH_4/H_2 flow ratio, as well as on chamber pressure during the synthesis. By varying these parameters, the intensity ratio of Raman D and G bands of graphene varied between ~1 and ~4, while the 2D to G band intensity ratio was found to be 0.05–0.5. Boundary defects are the most prominent defect type in PECVD graphene, giving it a grainy texture. Despite this, the samples exhibited sheet resistance values as low as 1.87 kΩ/□. This reveals great potential for PECVD methods and could contribute toward efficient and straightforward graphene growth on various substrates.

Keywords: graphene; PECVD; sapphire; sheet resistance

1. Introduction

High charge carrier mobility, mechanical strength and optical transparency are the properties that make graphene standout from other materials developed for high-speed electronics [1], solar cell [2] and sensor [3] applications. For example, the graphene/dielectric interface shows a lot of promise for sensing devices. Temperature sensors based on the graphene/SiN configuration perform excellently and have a very fast response and mechanical stability [4]. Graphene can also be used in magnetoresistance sensors, which are optimal in the 0.1–20 T range, when grown on polycrystalline Al_2O_3 substrates [5]. The peculiar nature of graphene in humidity and carbon dioxide sensing was also investigated when SiO_2 and sapphire substrates were selected [6]. It has been shown that device performance also relies on the substrate used, not only the quality of the graphene. Despite this, most concepts utilize exfoliated graphene, due to its quality (low defect density) [3,7,8]. However, exfoliation fails when large-area deposition is required [9,10]. Chemical vapor deposition (CVD) synthesis methods are far superior when it comes to graphene scalability [11–13]. To maintain the pristine quality of graphene in terms of defect density and domain (flake) size, most CVD methods focus on synthesis that requires Cu or other types of metal catalyst films [14–16]. The extra transfer step has to be taken into account for the proper utilization of graphene on desired substrates. The transfer of graphene from catalytic surfaces onto various substrates is quite complicated [17,18] and usually results in unwanted contamination, cracking or even the destruction of the initial graphene film [19,20]. Changing the growth

parameters and experimenting with different substrates might produce better results. For example, it was shown that graphene can be grown directly on SiC, with high charge carrier mobility and the ability to tune graphene properties by varying the doping amounts [21]. Similarly, there have been attempts to synthesize graphene on a Si(100) and SiO_2 substrate directly, using plasma-enhanced chemical vapor deposition (PECVD) [22–24]. In this way, graphene synthesis temperatures were significantly reduced (below 700 °C). However, directly synthesized graphene is nanocrystalline, and boundary defects dominate such samples [25,26].

During the last decade, there have been attempts to synthesize graphene on Al_2O_3 substrates [27–31], and particular attention was given to C-plane sapphire substrates [32–34]. Having a catalytic nature, C-plane sapphire ensures a more stable growth process, eliminates the unwanted grain boundary effects and significantly increases the size of graphene crystallites, due to the naturally matched hexagonal graphene and sapphire structures [35]. Recent reports indicate the enormous potential of graphene/C-plane sapphire interface. Wafer-scale, highly oriented graphene, exhibiting high carrier mobility and low sheet resistance, was directly grown on sapphire [36]. Sapphire is also an excellent substrate for GaN remote epitaxy assisted by a graphene interlayer; in this case, directly grown graphene is more beneficial than transferred graphene [37]. It has been recently shown that graphene synthesis can also be activated using Al-enriched C-plane sapphire substrates [38]. However, high quality films have only been produced using CVD, where temperatures well above 1000 °C are required [36]. The use of the PECVD would allow us to substantially decrease the temperature of synthesis. However, only a handful of studies have been performed on direct catalyst-less graphene growth on sapphire substrate using PECVD [39–41]. The use of PECVD provides an additional opportunity to control the graphene synthesis conditions. However, in the case of graphene PECVD synthesis on sapphire, only the effects of hydrogen and acetylene gas flows on the graphene structure were studied [39].

In this research, the effects of the graphene synthesis pressure and the ratio of hydrogen to methane gas flows were investigated. We show a way to couple both substrate catalytic effects and low-temperature synthesis mechanisms to make graphene growth on C-plane sapphire substrates more efficient and cost-effective. The small chamber size and the ability to change the synthesis conditions in a wide range of parameters provide versatility for further industrial development prospects. Paired with the ability to produce fairly low-resistance graphene films, this method could be considered as a viable option for sensing applications.

2. Materials and Methods

The synthesis of graphene/C-plane sapphire samples was performed using a microwave PECVD system, Cyrannus (Innovative Plasma Systems (Iplas) GmbH, Troisdorf, Germany). Monocrystalline, double-side-polished, $10 \times 10 \times 0.5$ mm C-plane (0001) sapphire (AdValue Technology, Tuscon, AZ, USA) was used as a substrate for all samples (Figure 1a). The synthesis was carried out in a similar way to our previous work [42,43]. A schematic of our growth stages is depicted in Figure 1d. A mixture of hydrogen and methane was used as the precursor gas in all cases. Initially, plasma was ignited using hydrogen gas until the target temperature was reached. After that, a 10 min. H_2 plasma annealing phase followed , where the flow of H_2 was set to 200 sccm. Hereinafter, the H_2 flow was reduced, and methane was introduced into the chamber according to the selected growth condition. We produced two separate sample sets. A set, named F, consisted of samples where different CH_4 gas flows were used, keeping the sum of CH_4 and H_2 gas flows at 100 sccm and leaving other parameters fixed. Another set, named P, consisted of samples where the pressure was changed for each synthesis, while maintaining the CH_4/H_2 gas-flow ratio (35/65 sccm) and keeping the other parameters fixed. Additionally, three more samples were synthesized in order to populate the gas-flow ratio and pressure-space colormaps (set named S). The synthesis conditions of all graphene/C-plane sapphire

samples can be seen in Table 1. To prevent excessive direct plasma action during each graphene synthesis process, C-plane sapphire substrates were covered with a protective steel enclosure, as seen in Figure 1a.
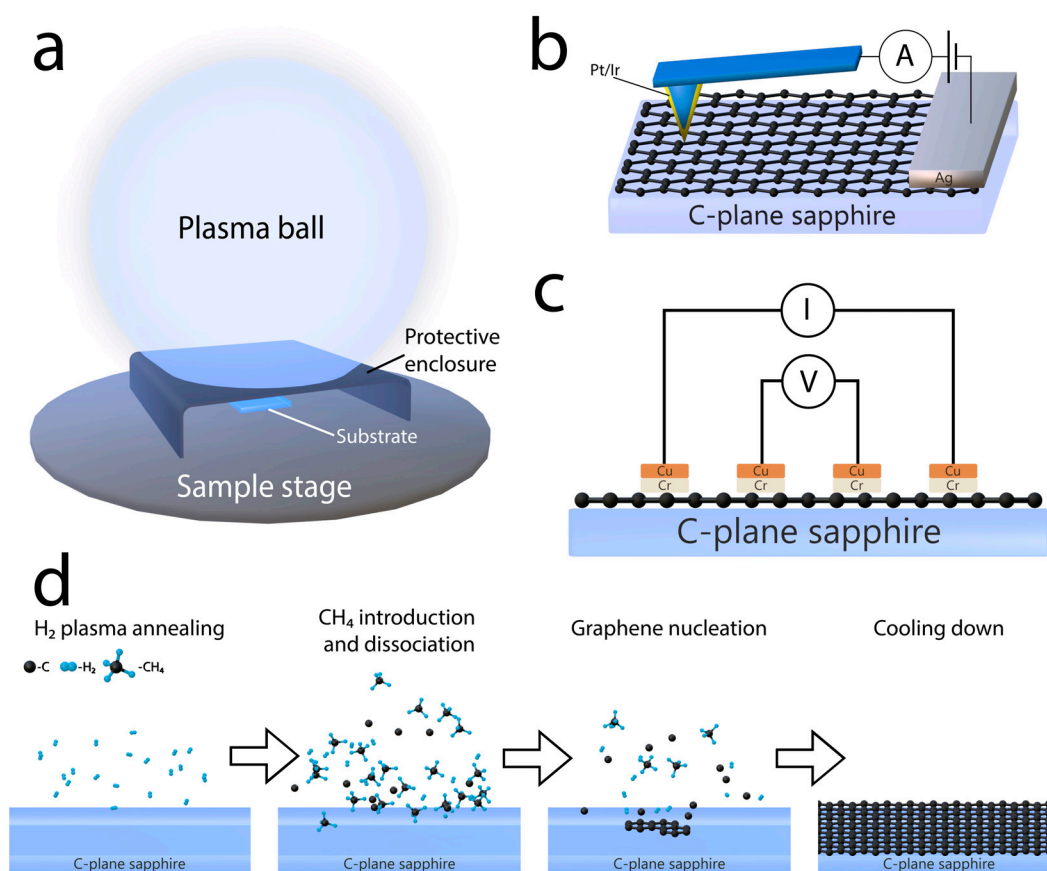

Figure 1. (**a**) Schematic of the PECVD chamber during graphene synthesis on C-sapphire substrate, (**b**) illustration of C-AFM analysis, (**c**) illustration of four-point probe analysis for sheet resistance measurement and (**d**) schematic representation of PECVD graphene synthesis stages. Atom spacing, electrode placement and dimensions are not to scale for clarity.

Table 1. Synthesis conditions for investigated graphene/C-plane sapphire samples. Note that the sample F3P2 belongs to the F and P sets.

Set	Sample No.	Power, kW	H_2, sccm	CH_4, sccm	p, mBar	T, °C	t, min.
	F1	0.7	75	25	10	700	60
	F2	0.7	70	30	10	700	60
F	F3P2	0.7	65	35	10	700	60
	F4	0.7	60	40	10	700	60
	F5	0.7	55	45	10	700	60
	P1	0.7	65	35	6	700	60
	F3P2	0.7	65	35	10	700	60
P	P3	0.7	65	35	15	700	60
	P4	0.7	65	35	20	700	60
	P5	0.7	65	35	25	700	60
	S1	0.7	80	20	6	700	60
S	S2	0.7	75	25	6	700	60
	S3	0.7	75	25	25	700	60

The graphene structure was analyzed using Raman scattering spectroscopy (Renishaw inVia microscope, Wotton-under-Edge, UK). The excitation wavelength for all measure-

ments was 532 nm, and a beam power of 1.5 mW was used. Five measurements were performed for each sample just after the synthesis of graphene films, to average the structural effects across the sample. For the detection of graphene fingerprint, the main D peak at ~1350 cm^{-1}, G peak at ~1600 cm^{-1} and 2D peak at ~2700 cm^{-1} were analyzed and fitted using a Lorentzian function [44]. Defects were analyzed using the D and G peak intensity ratio (I_D/I_G) [44–46], while the thickness of graphene was determined using the 2D and G peak intensity ratio (I_{2D}/I_G) [47]. Strain and doping were investigated using the position and full-width at half maximum (FWHM) of the peaks [46,48].

The surface conductivity and morphology of the directly synthesized graphene sheets were analyzed by atomic force microscopy (NanoWizard®3, JPK Instruments, Bruker Nano GmbH, Berlin, Germany). The morphology images of each sample were collected using an ACTA (Applied NanoStructures, Inc., Mountain View, CA, USA) probe operating in tapping mode. The probe tip radius of curvature was 6 nm. The conductivity was measured using contact-mode conductive atomic force microscopy (C-AFM) with a metal-coated tip ANSCM-PT (AppNano, Mountain View, CA, USA) silicon probe with a thin layer of Pt/Ir coating (thickness (nm) -25 ± 5) on both the reflex and tip sides of the probe. ANSCM probes with a 1.6 spring constant are ideal for use in C-AFM mode (as shown in Figure 1b). Tip shape: tetrahedral; tip ROC (nm): 30; height (μm): 14–16; frequency (kHz): 61. The electrical current was measured as a function of the applied bias voltage (-10–10 mV). All the measurements were performed at room temperature in the air [49].

To test resistive characteristics, samples F2, F5, P1, P5 were selected. A horizontal row of rectangular 2×1 mm contacts, which are spaced 1 mm apart, was deposited on the graphene/C-plane sapphire. Electrical contacts were made from Cr and Cu with thicknesses of 20 and 200 nm, respectively. The samples were analyzed with the GOM-805 DC Milli-Ohm Meter (GW Instek, New Taipei City, Taiwan), using the four-point probe method at ambient pressure and room temperature, as shown in Figure 1c. The acquired resistance values were corrected for the geometry and arrangement of the contacts.

3. Results

First, we compare graphene synthesized using MW-PECVD on a C-plane Al_2O_3, along with graphene grown on SiO_2. Most of the samples grown on C-plane sapphire exhibited a wide luminescence background at ~2000 cm^{-1}, which had to be subtracted. It was concluded that the substrate was the source of the background in all Raman spectra (Figure S1). The typical, baseline-corrected Raman spectra of the samples grown on C-plane sapphire can be seen in Figure 2a, along with a typical spectrum of graphene synthesized on SiO_2. Graphene fingerprints are clearly seen, with 2D (~2690 cm^{-1}), G (~1595 cm^{-1}) and D (~1350 cm^{-1}) peaks visible in all spectra. This has also been reported in similar studies, in which graphene was synthesized on Al_2O_3 [27,50,51] and SiO_2 substrates [52–54]. An apparent blueshift of the D and G peaks is visible in the graphene grown on C-plane sapphire as compared to the graphene grown on SiO_2. Furthermore, an in-depth analysis of the graphene synthesized on C-plane sapphire was performed. The thickness of the films can be discovered from the I_{2D}/I_G relation [55,56]. In our case, when the CH_4/H_2 ratio of 35/65 sccm was used and the pressure was set to 6 mBar, I_{2D}/I_G was 0.68, which indicates a few-layered graphene film as compared to the case of 25 mBar, where I_{2D}/I_G was 0.09, indicating a multilayer graphene film. A summary of I_{2D}/I_G and I_D/I_G with respect to different gas-flow ratios and chamber pressures used is shown in Figure 2b,d. The contour plot was interpolated from the points, with two cross sections indicating pressure and precursor gas-flow ratio parameter sweeps (Figure 2b,d: green and blue points, along with the red intersecting point). Increasing pressure ultimately increases I_{2D}/I_G, and a similar increase is observed with increased CH_4/H_2 gas flow. We also consider the I_D/I_G ratio, which reveals grain boundary defects [57] (Figure 2d). We show that the number of defects increases with a decrease in pressure and the CH_4/H_2 flow ratio, and it correlates linearly with I_{2D}/I_G (Figure 2c). A large increment in the growth conditions introduced a lot of variability in our reported I_D/I_G and I_{2D}/I_G values. The distribution of values across a

single sample may be associated with the inability to control certain synthesis elements, such as plasma homogeneity and substrate placement in the chamber prior to growth. This relation suggests that graphene grows more disorderly when the graphene thickness is low. As we approach thicker graphene films, the structure of samples tends to be more uniform. This might be attributed to higher amounts of boundary defects, which indicate a rather polycrystalline graphene film, as previously reported [43]. Similar conclusions can be drawn based on Raman theory [58,59]. When observing the $I_D/I_{D'}$ data with respect to the synthesis conditions used (Figure S2a,b), most of our samples exhibit boundary-like defects associated with the nanocrystalline nature of our samples, where $I_D/I_{D'}$—~3.5. Only when we drastically increase the gas-flow ratio and pressure, the value of $I_D/I_{D'}$ reduces to ~2.6, indicating a superposition of boundary and on-site defects. This could occur due to the increase in the byproducts of dissociation, when the pressure and CH_4 content are higher. When the synthesis pressure is lower, we can see vacancy and boundary defect superposition, which result from the poor nucleation of carbon atoms at the C-plane sapphire surface.
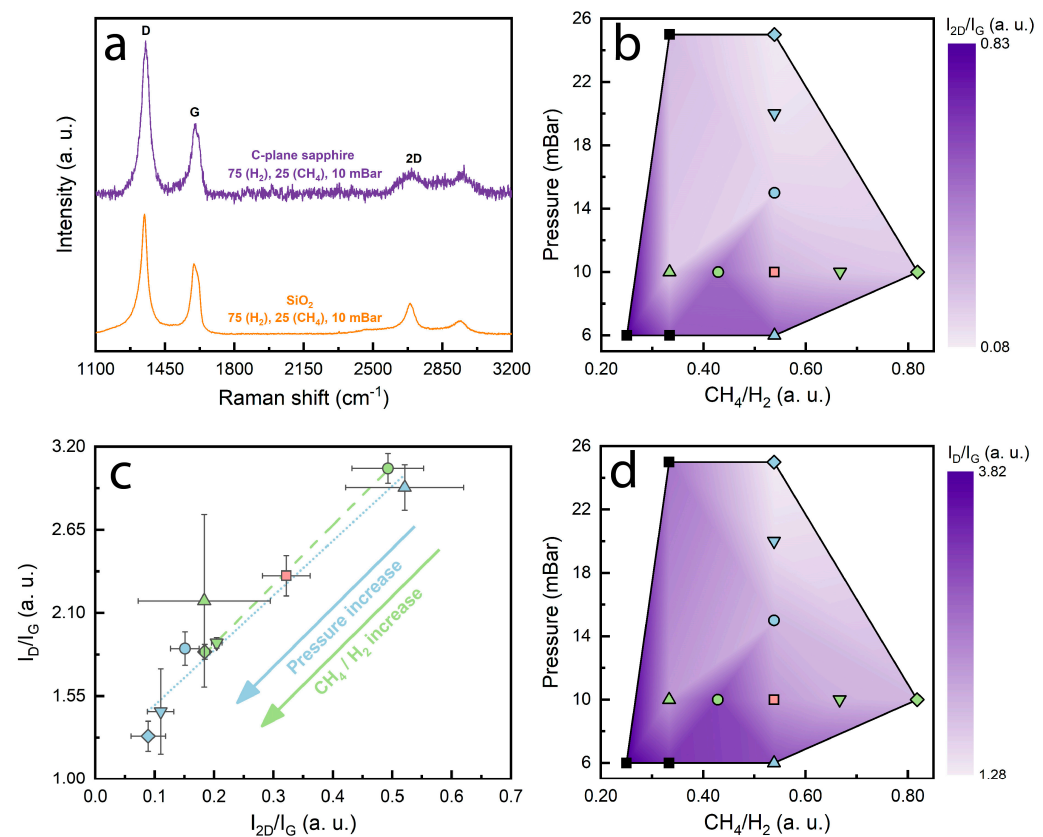

Figure 2. (**a**) Comparison of Raman spectra of PECVD graphene on C−plane sapphire (violet) and SiO₂ (orange), (**b**) colormap of I_{2D}/I_G ratio vs. synthesis parameters, (**c**) I_D/I_G ratio vs. I_{2D}/I_G ratio, (**d**) colormap of I_D/I_G ratio vs. synthesis parameters. The samples were differentiated by shapes and color, where light green represents samples that belong to the F set and light blue represents samples that belong to the P set. Sample F3P2, which belongs to both sets, is colored red. Additional samples were produced (set S) for colormap space expansion.

To assess the effects induced by strain, the 2D peak position and its full width at half maximum (FWHM$_{2D}$) were considered [38,60–62] (Figure 3). Although the distribution of the 2D peak position is broad when the CH_4/H_2 flow ratio of 25/75 is used, there is a clear decrease in the 2D peak position values (from 2702 cm^{-1} to 2694 cm^{-1}) when the precursor gas-flow ratio increases further (Figure 3a). This is in agreement with other reports from similar studies [30,34] and can be attributed to the stress induced in the graphene structure after the deposition process due to the thermal expansion coefficient mismatch [61,62].

$FWHM_{2D}$ is high in all cases, increasing from ~70 cm^{-1} to ~180 cm^{-1} when the CH_4/H_2 flow ratio is increased (Figure 3c). Multilayer graphene must be considered, and the change might be directly related to the increase in carbon species during deposition [63,64]. Ultimately, it shows a non-uniform strain distribution in all of our samples [38]. In contrast, when we increase the chamber pressure, the deviation of the 2D peak position increases, while the values remain similar (Figure 3c). There is no correlation between $FWHM_{2D}$ and changes in chamber pressure, as seen in Figure 3d.
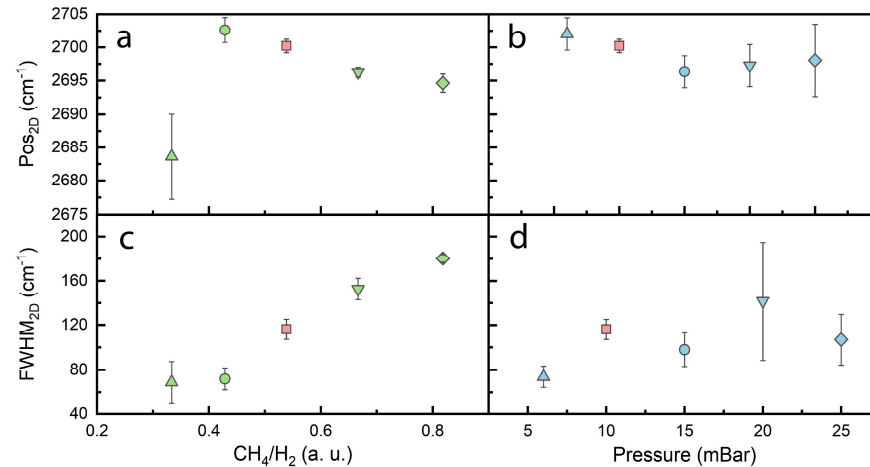

Figure 3. (**a**) Pos_{2D} vs. gas-flow ratio plot, (**b**) Pos_{2D} vs. pressure plot, (**c**) $FWHM_{2D}$ vs. gas-flow ratio plot, (**d**) $FWHM_{2D}$ vs. pressure plot of F and P samples. Conveniently, samples were given the same shapes and colors for distinction.

Furthermore, the effects of strain and doping were investigated using the Pos_{2D} vs. Pos_G plot (Figure 4) [62,65,66]. This established method suggests that most of our graphene samples are undoped or have a slight p-type doping. However, considering that most of our graphene samples are few-layered or thicker, these results may be inconclusive. Despite that, only several samples exhibit a higher Pos_G distribution. Vector decomposition analysis depicts the compressive strain present in most of our samples. Nevertheless, greater thickness might contribute to such observations, since the 2D peak position tends to blueshift with an increasing number of graphene layers [65,66].
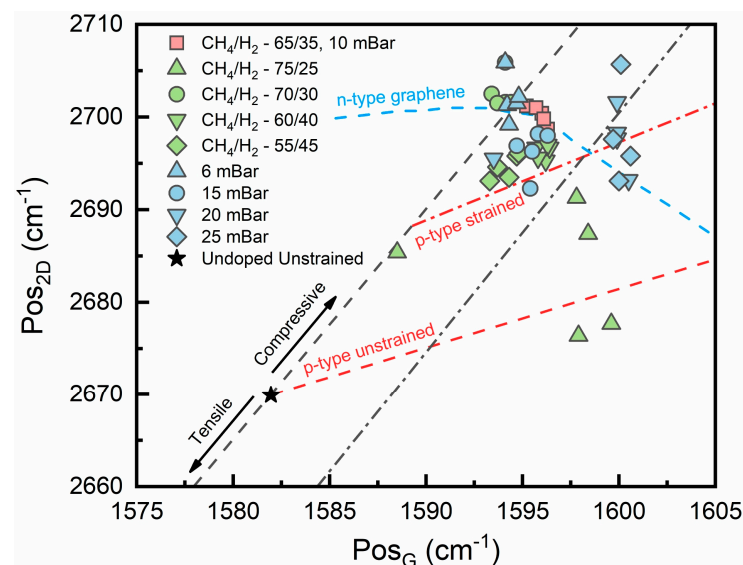

Figure 4. Pos_{2D} vs. Pos_G plot showing vector decomposition analysis of F and P sample sets. Conveniently, samples were given the same shapes and colors for distinction.

The surface morphology of graphene synthesized on C-plane sapphire was studied with atomic force microscopy. Graphene structures are grainy, albeit smooth. The root mean square roughness (R_q) of the samples was rather low, ranging from ~0.09 to 3.18 nm. The roughness of this size indicates the growth of planar graphene. The shared sample in both parameter sweeps had the lowest surface roughness (Figure 5a). It is important to note that the roughness of the pristine C-plane sapphire substrate was ~0.05 nm (Figure S3). The summarized roughness values according to CH_4/H_2 and pressure can be seen in Figure 5b,c, respectively. The produced graphene tends to become rougher with an increase in both the gas-flow ratio and pressure individually. Naturally, above certain gas-flow ratios and pressure threshold values, the surface roughness increases significantly. Low surface roughness was observed to correlate with higher I_{2D}/I_G values; however, it also increased the I_D/I_G ratio (Figure 6). Similar results have previously been observed with the synthesis of graphene performed on a Si(100) substrate [25]. It seems that the quality of graphene on the C-plane sapphire substrate is rather similar to the one that is grown on Si(100) substrate when using the MW-PECVD method. Temperatures well above 700 C might be required to achieve better quality graphene films on C-sapphire substrates, as reported by other studies [36,38]. Nevertheless, lower CH_4 flow and lower pressure favor higher quality graphene synthesis. AFM images of the produced samples can be seen in Figures S4–S12.
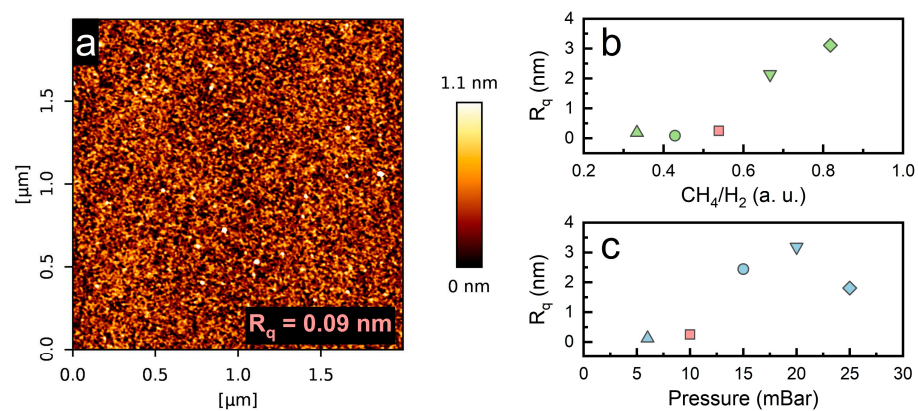

Figure 5. (**a**) Morphology of graphene synthesized using a CH_4/H_2 flow ratio of 35/65 and a pressure of 10 (R_q indicates the root mean square value of surface roughness), (**b**) R_q vs. gas-flow ratio plot, (**c**) R_q vs. pressure plot. The colors and shapes follow the same sample pattern.
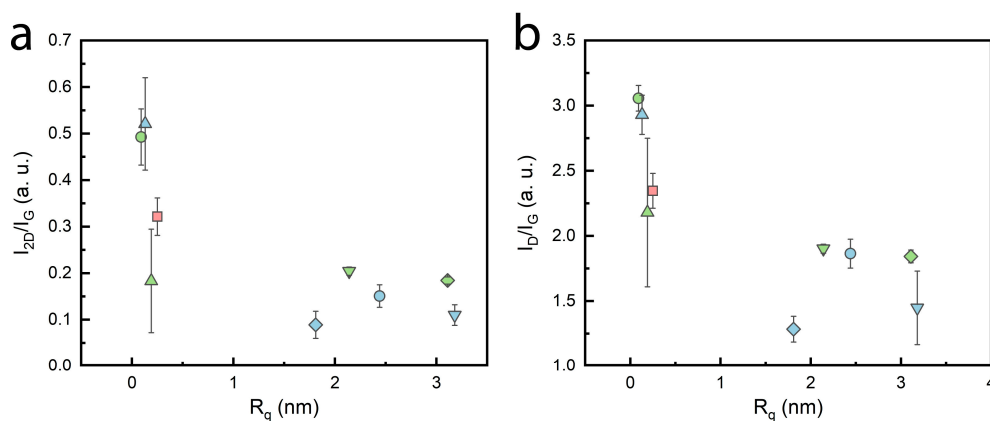

Figure 6. (**a**) Two-dimensional (2D) and G band ratio with respect to surface roughness, (**b**) plot showing correlation with surface roughness. The colors and shapes follow the same sample pattern.

Conductive atomic force microscopy measurements were performed to observe the electrical properties of the graphene films. As mentioned in the experimental section, four samples were analyzed, bearing the highest and lowest I_{2D}/I_G and I_D/I_G ratios (Figure 7).

Interestingly, most of the samples fell under the extremes of the chosen CH_4/H_2 gas-flow ratio and the experimental pressure sets. It seems that the growth conditions had a tremendous impact on the graphene current signal readouts. When the precursor gas-flow ratio was 30/70, the graphene exhibited the lowest current signals out of the four samples that were chosen, with a highest conductivity reaching 2.16 pA. When the gas-flow ratio was increased to 45/55, the current signal increased more than twentyfold, with the highest value being 51.9 pA. On the other hand, increasing the gas-flow ratio ultimately resulted in the thickest graphene sample. This would lead to the conclusion that we do not observe a monolayer, defect-free graphene effects when the thickness is low, knowing the highly conductive nature of pristine graphene [67]. The presence of graphene-like flakes or nanographene [68] could be observed and would explain the thickness-dependent increase in the current signal. We see a similar trend when pressure changes from 6 mBar to 25 mBar, where signal values change from 2.46 to 6.6 pA, respectively. It seems that the decrease in I_{2D}/I_G, seen in Figure 8a, is partly responsible for the increase in current signal. Similarly, the decrease in I_D/I_G also increases the current signal. In principle, higher amounts of intrinsic grain boundary defects should not decrease the charge carrier mobility; however, it could indicate an extrinsic grain boundary effect in our films, or low-symmetry grain boundaries, consisting of tilts and angle changes between the grains, which changes the electronic properties dramatically [69].
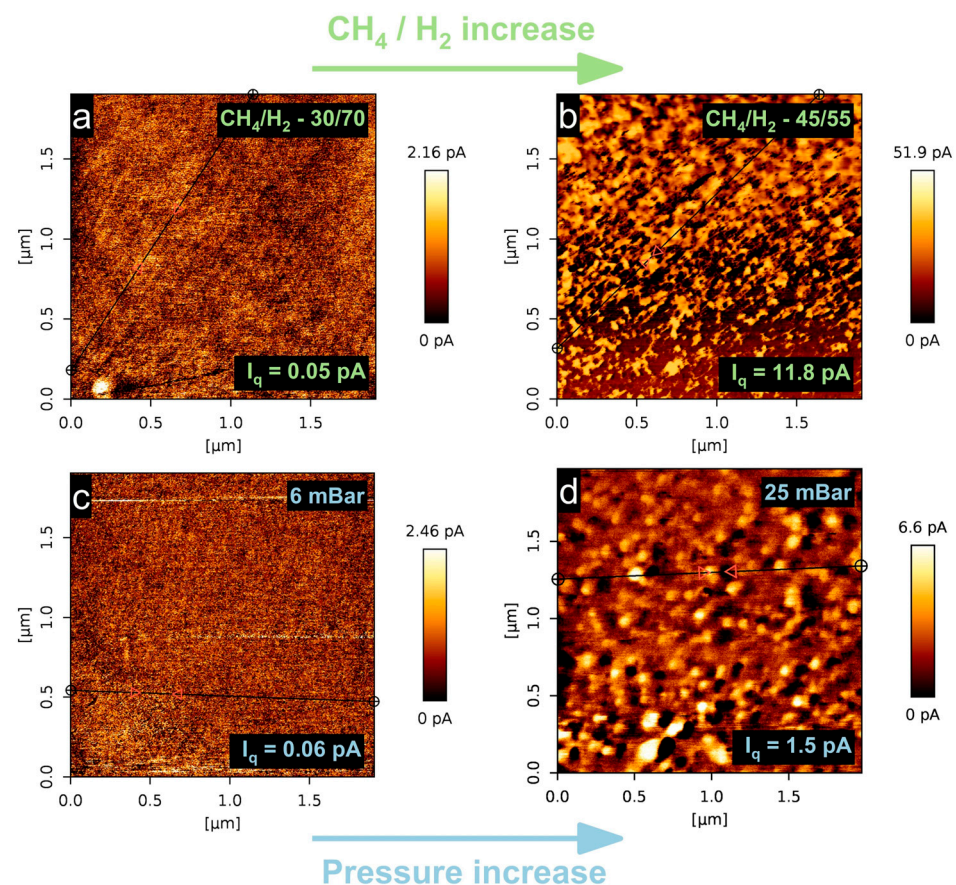

Figure 7. Conductive atomic force microscopy maps of four selected samples with varying synthesis conditions. (**a**) F2 sample, (**b**) F5 sample, (**c**) P1 sample, (**d**) P5 sample. I_q represents the root mean square of surface conductivity values.

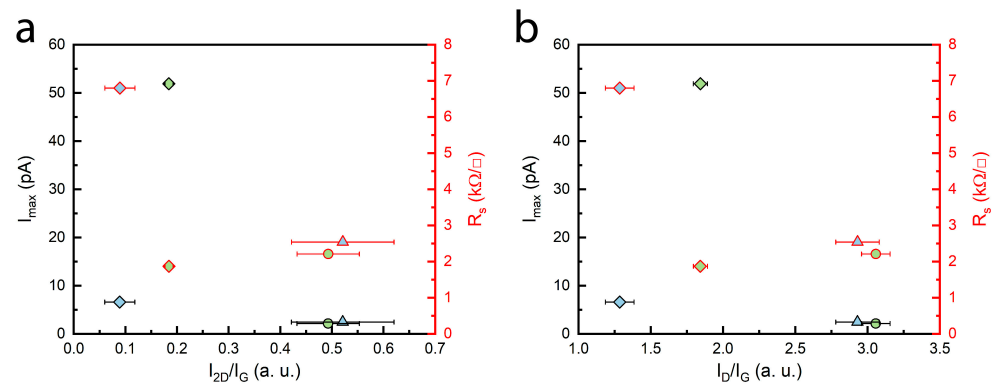**Figure 8.** (**a**) Resistance characteristics vs. I_{2D}/I_G plot showing conductance and sheet resistance variation with different thicknesses of graphene, (**b**) resistance characteristics vs. I_D/I_G plot showing conductance and sheet resistance variation based on defects.

The same four samples were further modified by synthesizing four, equally spaced, contacts, as mentioned in the experimental section, to determine the sheet resistance of the graphene films, using the four-point probe method. As seen in Figure 8, we can observe high R_s values when current signals acquired from conductive atomic force microscopy are low and rather low R_s values when current signals are high. In fact, the highest and lowest sheet resistance values were 6.8 kΩ/□ and 1.87 kΩ/□, respectively. The highest R_s value of the four was reported for the sample that was synthesized using a CH_4/H_2 ratio of 35/65 and a chamber pressure of 25 mBar. The lowest sheet resistance was observed when the sample was grown with a 45/55 gas-flow ratio and a chamber pressure of 10 mBar.

Our reported sheet resistance values are similar when compared to graphene synthesis on sapphire using other methods (see Table 2). It is evident that this growth method exhibits a lot of versatility with respect to structure and resistance characteristics, when considering graphene synthesis on Al_2O_3 for sensor applications. Further improvements in this synthesis method are necessary to obtain higher quality graphene films. The variability that is introduced in the structure across a film could be mitigated when plasma mechanisms occurring in the chamber are thoroughly examined. To fully understand the effects of protective enclosures, different types of enclosure materials must also be investigated.

Table 2. Sheet resistances measured for graphene on sapphire substrates.

Sample No.	Highest Surface Point, nm	Sheet Resistance, kΩ/□	Reference
A-plane sapphire	Low-pressure CVD	0.728	[29]
C-plane sapphire	Electron cyclotron resonance CVD	0.95	[39]
C-plane sapphire	High-temperature CVD	~1	[32]
Sapphire	Critical PECVD	4.1	[40]
C-plane sapphire	PECVD	1.87	This study

4. Conclusions

We have shown a novel approach to low-temperature, transfer-less graphene deposition that involves plasma-enhanced chemical vapor deposition. The quality of graphene can be varied by adjusting the pressure and the CH_4/H_2 gas-flow ratio, with I_D/I_G values ranging from ~1 to ~4. The surface roughness of graphene mimics that of a substrate when low gas-flow ratios and chamber pressures are used. There is a notable reduction in the quality of graphene as a result of boundary defects and a grainy structure. Such a deposition evolves from poor nucleation. Despite the deposition of what appears to be a grainy multilayer graphene film, the electrical properties tend to be superior when

compared to graphene synthesized using other CVD-based techniques. As a result, the sheet resistances can be as low as 1.87 kΩ/$\square$. To further improve this synthesis method, a thorough investigation of plasma-associated effects must be considered. Naturally, plasma shielding is an important part of this synthesis technique, and the protective enclosure effect has to be investigated in more detail. By limiting the variability governed by these factors, the homogeneity of graphene films should be greatly improved, allowing for direct quality assessment based on the synthesis conditions used.

Supplementary Materials: The following supporting information can be downloaded at: https://www.mdpi.com/article/10.3390/nano14201635/s1, Figure S1: Raw Raman spectra of C-plane sapphire and SiO_2 for comparison; Figure S2: Plot showing a dominant defect type associated with graphene grown using different synthesis conditions: (a) $I_D/I_{D'}$ vs. CH_4/H_2 gas-flow ratio and (b) $I_D/I_{D'}$ vs. chamber pressure, based on fitted data using Raman theory [58,59]. Conveniently, samples were given the same shapes and colors for distinction, as in the main text.; Figure S3: AFM image of C-plane sapphire substrate; Figure S4: AFM image of F1 sample; Figure S5: AFM image of F2 sample; Figure S6: AFM image of F3P2 sample; Figure S7: AFM image of F4 sample; Figure S8: AFM image of F5 sample; Figure S9: AFM image of P1 sample; Figure S10: AFM image of P3 sample; Figure S11: AFM image of P4 sample; Figure S12: AFM image of P5 sample.

Author Contributions: Conceptualization, A.G. and N.Ž.; software, Š.J.; investigation, Š.J. and A.G.; resources, A.G. and N.Ž.; data curation, Š.J. and A.G.; writing—original draft preparation, Š.J. and Š.M.; writing—review and editing, N.Ž., Š.M. and A.G.; visualization, Š.J.; supervision, N.Ž. and A.G.; project administration, N.Ž. and A.G.; funding acquisition, N.Ž. All authors have read and agreed to the published version of the manuscript.

Data Availability Statement: No new data were created or analyzed in this study. Data sharing is not applicable to this article.

Conflicts of Interest: The authors declare no conflicts of interest.

References

1. Liao, L.; Lin, Y.-C.; Bao, M.; Cheng, R.; Bai, J.; Liu, Y.; Qu, Y.; Wang, K.L.; Huang, Y.; Duan, X. High-Speed Graphene Transistors with a Self-Aligned Nanowire Gate. *Nature* **2010**, *467*, 305–308. [CrossRef] [PubMed]
2. Miao, X.; Tongay, S.; Petterson, M.K.; Berke, K.; Rinzler, A.G.; Appleton, B.R.; Hebard, A.F. High Efficiency Graphene Solar Cells by Chemical Doping. *Nano Lett.* **2012**, *12*, 2745–2750. [CrossRef]
3. Xia, F.; Mueller, T.; Lin, Y.; Valdes-Garcia, A.; Avouris, P. Ultrafast Graphene Photodetector. *Nat. Nanotechnol.* **2009**, *4*, 839–843. [CrossRef]
4. Davaji, B.; Cho, H.D.; Malakoutian, M.; Lee, J.-K.; Panin, G.; Kang, T.W.; Lee, C.H. A Patterned Single Layer Graphene Resistance Temperature Sensor. *Sci. Rep.* **2017**, *7*, 8811. [CrossRef]
5. Zurauskiene, N.; Lukose, R.; Balevicius, S.; Stankevic, V.; Kersulis, S.; Plausinaitiene, V.; Vagner, M.; Navickas, R. Compact Manganite-Graphene Magnetoresistive Sensor. *IEEE Magn. Lett.* **2019**, *10*, 8105605. [CrossRef]
6. Elgammal, K.; Hugosson, H.W.; Smith, A.D.; Råsander, M.; Bergqvist, L.; Delin, A. Density Functional Calculations of Graphene-Based Humidity and Carbon Dioxide Sensors: Effect of Silica and Sapphire Substrates. *Surf. Sci.* **2017**, *663*, 23–30. [CrossRef]
7. Zhang, B.Y.; Liu, T.; Meng, B.; Li, X.; Liang, G.; Hu, X.; Wang, Q.J. Broadband High Photoresponse from Pure Monolayer Graphene Photodetector. *Nat. Commun.* **2013**, *4*, 1811. [CrossRef]
8. Gan, X.; Shiue, R.-J.; Gao, Y.; Meric, I.; Heinz, T.F.; Shepard, K.; Hone, J.; Assefa, S.; Englund, D. Chip-Integrated Ultrafast Graphene Photodetector with High Responsivity. *Nat. Photonics* **2013**, *7*, 883–887. [CrossRef]
9. Yi, M.; Shen, Z. A Review on Mechanical Exfoliation for the Scalable Production of Graphene. *J. Mater. Chem. A Mater.* **2015**, *3*, 11700–11715. [CrossRef]
10. Coleman, J.N. Liquid Exfoliation of Defect-Free Graphene. *Acc. Chem. Res.* **2013**, *46*, 14–22. [CrossRef]
11. Li, X.; Cai, W.; An, J.; Kim, S.; Nah, J.; Yang, D.; Piner, R.; Velamakanni, A.; Jung, I.; Tutuc, E.; et al. Large-Area Synthesis of High-Quality and Uniform Graphene Films on Copper Foils. *Science* **2009**, *324*, 1312–1314. [CrossRef] [PubMed]
12. Deokar, G.; Avila, J.; Razado-Colambo, I.; Codron, J.-L.; Boyaval, C.; Galopin, E.; Asensio, M.-C.; Vignaud, D. Towards High Quality CVD Graphene Growth and Transfer. *Carbon N. Y.* **2015**, *89*, 82–92. [CrossRef]

13. Deng, B.; Liu, Z.; Peng, H. Toward Mass Production of CVD Graphene Films. *Adv. Mater.* **2019**, *31*, e1800996. [CrossRef]
14. Zhang, Y.; Zhang, L.; Zhou, C. Review of Chemical Vapor Deposition of Graphene and Related Applications. *Acc. Chem. Res.* **2013**, *46*, 2329–2339. [CrossRef]
15. Losurdo, M.; Giangregorio, M.M.; Capezzuto, P.; Bruno, G. Graphene CVD Growth on Copper and Nickel: Role of Hydrogen in Kinetics and Structure. *Phys. Chem. Chem. Phys.* **2011**, *13*, 20836. [CrossRef] [PubMed]
16. Gao, M.; Pan, Y.; Huang, L.; Hu, H.; Zhang, L.Z.; Guo, H.M.; Du, S.X.; Gao, H.-J. Epitaxial Growth and Structural Property of Graphene on Pt(111). *Appl. Phys. Lett.* **2011**, *98*, 033101. [CrossRef]
17. Ullah, S.; Yang, X.; Ta, H.Q.; Hasan, M.; Bachmatiuk, A.; Tokarska, K.; Trzebicka, B.; Fu, L.; Rummeli, M.H. Graphene Transfer Methods: A Review. *Nano Res.* **2021**, *14*, 3756–3772. [CrossRef]
18. Leong, W.S.; Wang, H.; Yeo, J.; Martin-Martinez, F.J.; Zubair, A.; Shen, P.-C.; Mao, Y.; Palacios, T.; Buehler, M.J.; Hong, J.-Y.; et al. Paraffin-Enabled Graphene Transfer. *Nat. Commun.* **2019**, *10*, 867. [CrossRef]
19. Liang, X.; Sperling, B.A.; Calizo, I.; Cheng, G.; Hacker, C.A.; Zhang, Q.; Obeng, Y.; Yan, K.; Peng, H.; Li, Q.; et al. Toward Clean and Crackless Transfer of Graphene. *ACS Nano* **2011**, *5*, 9144–9153. [CrossRef]
20. Haigh, S.J.; Gholinia, A.; Jalil, R.; Romani, S.; Britnell, L.; Elias, D.C.; Novoselov, K.S.; Ponomarenko, L.A.; Geim, A.K.; Gorbachev, R. Cross-Sectional Imaging of Individual Layers and Buried Interfaces of Graphene-Based Heterostructures and Superlattices. *Nat. Mater.* **2012**, *11*, 764–767. [CrossRef]
21. Strupinski, W.; Grodecki, K.; Wysmolek, A.; Stepniewski, R.; Szkopek, T.; Gaskell, P.E.; Grüneis, A.; Haberer, D.; Bozek, R.; Krupka, J.; et al. Graphene Epitaxy by Chemical Vapor Deposition on SiC. *Nano Lett.* **2011**, *11*, 1786–1791. [CrossRef] [PubMed]
22. Li, M.; Liu, D.; Wei, D.; Song, X.; Wei, D.; Wee, A.T.S. Controllable Synthesis of Graphene by Plasma-Enhanced Chemical Vapor Deposition and Its Related Applications. *Adv. Sci.* **2016**, *3*, 1600003. [CrossRef] [PubMed]
23. Rehman, M.A.; Park, S.; Khan, M.F.; Bhopal, M.F.; Nazir, G.; Kim, M.; Farooq, A.; Ha, J.; Rehman, S.; Jun, S.C.; et al. Development of Directly Grown-graphene–Silicon Schottky Barrier Solar Cell Using Co-doping Technique. *Int. J. Energy Res.* **2022**, *46*, 11510–11522. [CrossRef]
24. Kadam, K.D.; Rehman, M.A.; Kim, H.; Rehman, S.; Khan, M.A.; Patil, H.; Aziz, J.; Park, S.; Abdul Basit, M.; Khan, K.; et al. Enhanced and Passivated Co-Doping Effect of Organic Molecule and Bromine on Graphene/HfO$_2$/Silicon Metal–Insulator–Semiconductor (MIS) Schottky Junction Solar Cells. *ACS Appl. Energy Mater.* **2022**, *5*, 10509–10517. [CrossRef]
25. Meškinis, Š.; Vasiliauskas, A.; Guobienė, A.; Talaikis, M.; Niaura, G.; Gudaitis, R. The Direct Growth of Planar and Vertical Graphene on Si(100) via Microwave Plasma Chemical Vapor Deposition: Synthesis Conditions Effects. *RSC Adv.* **2022**, *12*, 18759–18772. [CrossRef]
26. Rehman, M.A.; Roy, S.B.; Akhtar, I.; Bhopal, M.F.; Choi, W.; Nazir, G.; Khan, M.F.; Kumar, S.; Eom, J.; Chun, S.-H.; et al. Thickness-Dependent Efficiency of Directly Grown Graphene Based Solar Cells. *Carbon N. Y.* **2019**, *148*, 187–195. [CrossRef]
27. Zhan, H.; Garrett, D.J.; Apollo, N.V.; Ganesan, K.; Lau, D.; Prawer, S.; Cervenka, J. Direct Fabrication of 3D Graphene on Nanoporous Anodic Alumina by Plasma-Enhanced Chemical Vapor Deposition. *Sci. Rep.* **2016**, *6*, 19822. [CrossRef]
28. Park, J.; Lee, J.; Choi, J.-H.; Hwang, D.K.; Song, Y.-W. Growth, Quantitative Growth Analysis and Applications of Graphene on γ-Al$_2$O$_3$ Catalysts. *Sci. Rep.* **2015**, *5*, 11839. [CrossRef] [PubMed]
29. Ueda, Y.; Maruyama, T.; Naritsuka, S. Effect of Growth Pressure on Graphene Direct Growth on an A-Plane Sapphire Substrate: Implications for Graphene-Based Electronic Devices. *ACS Appl. Nano Mater.* **2021**, *4*, 343–351. [CrossRef]
30. Wördenweber, H.; Karthäuser, S.; Grundmann, A.; Wang, Z.; Aussen, S.; Kalisch, H.; Vescan, A.; Heuken, M.; Waser, R.; Hoffmann-Eifert, S. Atomically Resolved Electronic Properties in Single Layer Graphene on α-Al$_2$O$_3$ (0001) by Chemical Vapor Deposition. *Sci. Rep.* **2022**, *12*, 18743. [CrossRef]
31. Chang, C.-J.; Tsai, P.-C.; Su, W.-Y.; Huang, C.-Y.; Lee, P.-T.; Lin, S.-Y. Layered Graphene Growth Directly on Sapphire Substrates for Applications. *ACS Omega* **2022**, *7*, 13128–13133. [CrossRef] [PubMed]
32. Fanton, M.A.; Robinson, J.A.; Puls, C.; Liu, Y.; Hollander, M.J.; Weiland, B.E.; LaBella, M.; Trumbull, K.; Kasarda, R.; Howsare, C.; et al. Characterization of Graphene Films and Transistors Grown on Sapphire by Metal-Free Chemical Vapor Deposition. *ACS Nano* **2011**, *5*, 8062–8069. [CrossRef] [PubMed]
33. Hwang, J.; Kim, M.; Campbell, D.; Alsalman, H.A.; Kwak, J.Y.; Shivaraman, S.; Woll, A.R.; Singh, A.K.; Hennig, R.G.; Gorantla, S.; et al. Van Der Waals Epitaxial Growth of Graphene on Sapphire by Chemical Vapor Deposition without a Metal Catalyst. *ACS Nano* **2013**, *7*, 385–395. [CrossRef] [PubMed]
34. Li, J.; Chen, M.; Samad, A.; Dong, H.; Ray, A.; Zhang, J.; Jiang, X.; Schwingenschlögl, U.; Domke, J.; Chen, C.; et al. Wafer-Scale Single-Crystal Monolayer Graphene Grown on Sapphire Substrate. *Nat. Mater.* **2022**, *21*, 740–747. [CrossRef]
35. Wang, G.; Zhao, Y.; Deng, Y.; Huang, W.; Fan, X.; Zhang, J.; Duan, R.; Sun, L. Lattice Selective Growth of Graphene on Sapphire Substrate. *J. Phys. Chem. C* **2015**, *119*, 426–430. [CrossRef]
36. Chen, Z.; Xie, C.; Wang, W.; Zhao, J.; Liu, B.; Shan, J.; Wang, X.; Hong, M.; Lin, L.; Huang, L.; et al. Direct Growth of Wafer-Scale Highly Oriented Graphene on Sapphire. *Sci. Adv.* **2021**, *7*, eabk0115. [CrossRef]
37. Chang, C.S.; Kim, K.S.; Park, B.-I.; Choi, J.; Kim, H.; Jeong, J.; Barone, M.; Parker, N.; Lee, S.; Zhang, X.; et al. Remote Epitaxial Interaction through Graphene. *Sci. Adv.* **2023**, *9*, eadj5379. [CrossRef]
38. Mishra, N.; Forti, S.; Fabbri, F.; Martini, L.; McAleese, C.; Conran, B.R.; Whelan, P.R.; Shivayogimath, A.; Jessen, B.S.; Buß, L.; et al. Wafer-Scale Synthesis of Graphene on Sapphire: Toward Fab-Compatible Graphene. *Small* **2019**, *15*, e1904906. [CrossRef]

39. Muñoz, R.; López-Elvira, E.; Munuera, C.; Carrascoso, F.; Xie, Y.; Çakıroğlu, O.; Pucher, T.; Puebla, S.; Castellanos-Gomez, A.; García-Hernández, M. Low T Direct Plasma Assisted Growth of Graphene on Sapphire and Its Integration in Graphene/MoS$_2$ Heterostructure-Based Photodetectors. *NPJ 2D Mater. Appl.* **2023**, *7*, 57. [CrossRef]

40. Wei, D.; Lu, Y.; Han, C.; Niu, T.; Chen, W.; Wee, A.T.S. Critical Crystal Growth of Graphene on Dielectric Substrates at Low Temperature for Electronic Devices. *Angew. Chem. Int. Ed.* **2013**, *52*, 14121–14126. [CrossRef]

41. Lozano, M.S.; Bernat-Montoya, I.; Angelova, T.I.; Mojena, A.B.; Díaz-Fernández, F.J.; Kovylina, M.; Martínez, A.; Cienfuegos, E.P.; Gómez, V.J. Plasma-Induced Surface Modification of Sapphire and Its Influence on Graphene Grown by Plasma-Enhanced Chemical Vapour Deposition. *Nanomaterials* **2023**, *13*, 1952. [CrossRef] [PubMed]

42. Jankauskas, Š.; Gudaitis, R.; Vasiliauskas, A.; Guobienė, A.; Meškinis, Š. The Graphene Structure's Effects on the Current-Voltage and Photovoltaic Characteristics of Directly Synthesized Graphene/n-Si(100) Diodes. *Nanomaterials* **2022**, *12*, 1640. [CrossRef] [PubMed]

43. Gudaitis, R.; Lazauskas, A.; Jankauskas, Š.; Meškinis, Š. Catalyst-Less and Transfer-Less Synthesis of Graphene on Si(100) Using Direct Microwave Plasma Enhanced Chemical Vapor Deposition and Protective Enclosures. *Materials* **2020**, *13*, 5630. [CrossRef] [PubMed]

44. Merlen, A.; Buijnsters, J.; Pardanaud, C. A Guide to and Review of the Use of Multiwavelength Raman Spectroscopy for Characterizing Defective Aromatic Carbon Solids: From Graphene to Amorphous Carbons. *Coatings* **2017**, *7*, 153. [CrossRef]

45. Malard, L.M.; Pimenta, M.A.; Dresselhaus, G.; Dresselhaus, M.S. Raman Spectroscopy in Graphene. *Phys. Rep.* **2009**, *473*, 51–87. [CrossRef]

46. Childres, I.; Jauregui, L.A.; Tian, J.; Chen, Y.P. Effect of Oxygen Plasma Etching on Graphene Studied Using Raman Spectroscopy and Electronic Transport Measurements. *New J. Phys.* **2011**, *13*, 025008. [CrossRef]

47. Hwang, J.-S.; Lin, Y.-H.; Hwang, J.-Y.; Chang, R.; Chattopadhyay, S.; Chen, C.-J.; Chen, P.; Chiang, H.-P.; Tsai, T.-R.; Chen, L.-C.; et al. Imaging Layer Number and Stacking Order through Formulating Raman Fingerprints Obtained from Hexagonal Single Crystals of Few Layer Graphene. *Nanotechnology* **2013**, *24*, 015702. [CrossRef]

48. Casiraghi, C.; Pisana, S.; Novoselov, K.S.; Geim, A.K.; Ferrari, A.C. Raman Fingerprint of Charged Impurities in Graphene. *Appl. Phys. Lett.* **2007**, *91*, 233108. [CrossRef]

49. Meškinis, Š.; Gudaitis, R.; Vasiliauskas, A.; Guobienė, A.; Jankauskas, Š.; Stankevič, V.; Keršulis, S.; Stirkė, A.; Andriukonis, E.; Melo, W.; et al. Biosensor Based on Graphene Directly Grown by MW-PECVD for Detection of COVID-19 Spike (S) Protein and Its Entry Receptor ACE2. *Nanomaterials* **2023**, *13*, 2373. [CrossRef]

50. Song, H.J.; Son, M.; Park, C.; Lim, H.; Levendorf, M.P.; Tsen, A.W.; Park, J.; Choi, H.C. Large Scale Metal-Free Synthesis of Graphene on Sapphire and Transfer-Free Device Fabrication. *Nanoscale* **2012**, *4*, 3050. [CrossRef]

51. Zheng, S.; Zhong, G.; Wu, X.; D'Arsiè, L.; Robertson, J. Metal-Catalyst-Free Growth of Graphene on Insulating Substrates by Ammonia-Assisted Microwave Plasma-Enhanced Chemical Vapor Deposition. *RSC Adv.* **2017**, *7*, 33185–33193. [CrossRef]

52. Kim, Y.S.; Joo, K.; Jerng, S.-K.; Lee, J.H.; Yoon, E.; Chun, S.-H. Direct Growth of Patterned Graphene on SiO$_2$ Substrates without the Use of Catalysts or Lithography. *Nanoscale* **2014**, *6*, 10100–10105. [CrossRef] [PubMed]

53. Vishwakarma, R.; Rosmi, M.S.; Takahashi, K.; Wakamatsu, Y.; Yaakob, Y.; Araby, M.I.; Kalita, G.; Kitazawa, M.; Tanemura, M. Transfer Free Graphene Growth on SiO$_2$ Substrate at 250 °C. *Sci. Rep.* **2017**, *7*, 43756. [CrossRef] [PubMed]

54. Xu, S.C.; Man, B.Y.; Jiang, S.Z.; Chen, C.S.; Yang, C.; Liu, M.; Gao, X.G.; Sun, Z.C.; Zhang, C. Direct Synthesis of Graphene on SiO$_2$ Substrates by Chemical Vapor Deposition. *CrystEngComm* **2013**, *15*, 1840. [CrossRef]

55. Gupta, A.; Chen, G.; Joshi, P.; Tadigadapa, S. Eklund Raman Scattering from High-Frequency Phonons in Supported *n*-Graphene Layer Films. *Nano Lett.* **2006**, *6*, 2667–2673. [CrossRef] [PubMed]

56. Cho, J.H.; Gorman, J.J.; Na, S.R.; Cullinan, M. Growth of Monolayer Graphene on Nanoscale Copper-Nickel Alloy Thin Films. *Carbon N. Y.* **2017**, *115*, 441–448. [CrossRef]

57. Ferrari, A.C.; Basko, D.M. Raman Spectroscopy as a Versatile Tool for Studying the Properties of Graphene. *Nat. Nanotechnol.* **2013**, *8*, 235–246. [CrossRef]

58. Eckmann, A.; Felten, A.; Mishchenko, A.; Britnell, L.; Krupke, R.; Novoselov, K.S.; Casiraghi, C. Probing the Nature of Defects in Graphene by Raman Spectroscopy. *Nano Lett.* **2012**, *12*, 3925–3930. [CrossRef]

59. Venezuela, P.; Lazzeri, M.; Mauri, F. Theory of Double-Resonant Raman Spectra in Graphene: Intensity and Line Shape of Defect-Induced and Two-Phonon Bands. *Phys. Rev. B* **2011**, *84*, 035433. [CrossRef]

60. Ni, Z.H.; Yu, T.; Lu, Y.H.; Wang, Y.Y.; Feng, Y.P.; Shen, Z.X. Uniaxial Strain on Graphene: Raman Spectroscopy Study and Band-Gap Opening. *ACS Nano* **2008**, *2*, 2301–2305. [CrossRef]

61. Yoon, D.; Son, Y.-W.; Cheong, H. Negative Thermal Expansion Coefficient of Graphene Measured by Raman Spectroscopy. *Nano Lett.* **2011**, *11*, 3227–3231. [CrossRef] [PubMed]

62. Neumann, C.; Reichardt, S.; Venezuela, P.; Drögeler, M.; Banszerus, L.; Schmitz, M.; Watanabe, K.; Taniguchi, T.; Mauri, F.; Beschoten, B.; et al. Raman Spectroscopy as Probe of Nanometre-Scale Strain Variations in Graphene. *Nat. Commun.* **2015**, *6*, 8429. [CrossRef]

63. Ni, Z.; Wang, Y.; Yu, T.; You, Y.; Shen, Z. Reduction of Fermi Velocity in Folded Graphene Observed by Resonance Raman Spectroscopy. *Phys. Rev. B* **2008**, *77*, 235403. [CrossRef]

64. Ferrari, A.C.; Meyer, J.C.; Scardaci, V.; Casiraghi, C.; Lazzeri, M.; Mauri, F.; Piscanec, S.; Jiang, D.; Novoselov, K.S.; Roth, S.; et al. Raman Spectrum of Graphene and Graphene Layers. *Phys. Rev. Lett.* **2006**, *97*, 187401. [CrossRef]

65.   Lee, J.E.; Ahn, G.; Shim, J.; Lee, Y.S.; Ryu, S. Optical Separation of Mechanical Strain from Charge Doping in Graphene. *Nat. Commun.* **2012**, *3*, 1024. [CrossRef] [PubMed]

66.   Kim, S.; Ryu, S. Thickness-Dependent Native Strain in Graphene Membranes Visualized by Raman Spectroscopy. *Carbon N. Y.* **2016**, *100*, 283–290. [CrossRef]

67.   Morozov, S.V.; Novoselov, K.S.; Katsnelson, M.I.; Schedin, F.; Elias, D.C.; Jaszczak, J.A.; Geim, A.K. Giant Intrinsic Carrier Mobilities in Graphene and Its Bilayer. *Phys. Rev. Lett.* **2008**, *100*, 016602. [CrossRef]

68.   Yang, W.; He, C.; Zhang, L.; Wang, Y.; Shi, Z.; Cheng, M.; Xie, G.; Wang, D.; Yang, R.; Shi, D.; et al. Growth, Characterization, and Properties of Nanographene. *Small* **2012**, *8*, 1429–1435. [CrossRef]

69.   Zhang, H.; Lee, G.; Gong, C.; Colombo, L.; Cho, K. Grain Boundary Effect on Electrical Transport Properties of Graphene. *J. Phys. Chem. C* **2014**, *118*, 2338–2343. [CrossRef]